
Forest-Guided Semantic Transport for Label-Supervised Manifold Alignment

Adrien Aumon^{1,2*} Myriam Lizotte^{1,2*} Guy Wolf^{1,2} Kevin R. Moon³ Jake S. Rhodes⁴

Abstract

Label-supervised manifold alignment bridges the gap between unsupervised and correspondence-based paradigms by leveraging shared label information to align multimodal datasets. Still, most existing methods rely on Euclidean geometry to model intra-domain relationships. This approach can fail when features are only weakly related to the task of interest, leading to noisy, semantically misleading structure and degraded alignment quality. To address this limitation, we introduce FoSTA (Forest-guided Semantic Transport Alignment), a scalable alignment framework that leverages forest-induced geometry to denoise intra-domain structure and recover task-relevant manifolds prior to alignment. FoSTA builds semantic representations directly from label-informed forest affinities and aligns them via fast, hierarchical semantic transport, capturing meaningful cross-domain relationships. Extensive comparisons with established baselines demonstrate that FoSTA improves correspondence recovery and label transfer on synthetic benchmarks and delivers strong performance in practical single-cell applications, including batch correction and biological conservation.

1. Introduction

Manifold alignment seeks a shared representation for datasets collected in different modalities or feature spaces, and is a key primitive in multimodal learning and single-cell integration (Ham et al., 2003; 2005; Hie et al., 2019). Most approaches fall into two broad families: *semi-supervised* methods that rely on a set of known cross-domain correspondences (anchors) (Wang & Mahadevan, 2008; Duque et al., 2023b), and *unsupervised* methods that assume no shared

information and instead match domains using geometric or distributional structure (Mémoli, 2011; Demetci et al., 2022). In many practical settings, however, pointwise correspondences are impossible or expensive to obtain, while weaker side information—like shared class labels—is readily available (e.g., curated cell types across batches (Cao et al., 2021)). This motivates *label-supervised* manifold alignment, which uses labels to guide cross-domain matching without using anchors (Wang & Mahadevan, 2011; Tuia & Camps-Valls, 2016; Duque et al., 2023a).

Most label-supervised alignment methods rely on Euclidean geometry to model intra-domain structure. This fails when only a subset of features is relevant to the task, as Euclidean distances weigh all coordinates equally, mixing signal with nuisance variation. In high-dimensional settings, this creates misleading neighborhoods that degrade the alignment. Tree ensemble affinities offer a principled alternative by adaptively emphasizing label-relevant structure. In particular, RF-GAP proximities (Rhodes et al., 2023b) have been shown to outperform standard forest-based proximities and class-conditional Euclidean kernels in guided representation learning (Rhodes et al., 2023b;a; Aumon et al., 2025). However, their application to manifold alignment remains limited: existing formulations (Rhodes & Rustad, 2024b) require fully labeled domains or known correspondence anchors, making them unsuitable for the general label-supervised setting under partial label assignment.

To address these limitations, we introduce **FoSTA** (Forest-guided **S**emantic **T**ransport **A**lignment), a scalable framework that replaces Euclidean geometry with adaptive forest-based affinities and avoids the computational bottleneck of dense optimal transport (OT). A central contribution of our work is a semi-supervised extension of RF-GAP proximities (Rhodes et al., 2023b). This formulation constructs task-relevant geometries even when labels are partially available, allowing unlabeled samples to participate in the structure while still benefiting from available supervision. Using these affinities, FoSTA first derives compact semantic representations directly from the forest structure. It then leverages these shared representations to infer cross-domain correspondences via Hierarchical Refinement (HiRef; Halmos et al. (2025)), a fast implicit OT solver that avoids computing prohibitive pairwise costs between domains. Finally, FoSTA propagates these matches to learn smooth

*Equal contribution ¹Department of Mathematics and Statistics, Université de Montréal, Montreal, Canada ²Mila - Quebec AI Institute, Montreal, Canada ³Department of Mathematics and Statistics, Utah State University, Logan, Utah, USA ⁴Department of Statistics, Brigham Young University, Provo, Utah, USA. Correspondence to: Jake S. Rhodes <rhodes@stat.byu.edu>.

cross-domain affinities for joint embedding. On synthetic benchmarks with ground-truth anchors, FoSTA improves correspondence recovery and label transfer compared to established baselines (Wang & Mahadevan, 2011; Tuia & Camps-Valls, 2016; Duque et al., 2023a; Cao et al., 2021). In single-cell integration tasks lacking known correspondences, it achieves strong batch correction while preserving biological signal, outperforming competitors on standard integration metrics.

2. Background

2.1. Guided manifold learning with tree ensembles

Manifold learning methods traditionally rely on unsupervised, Euclidean-based kernels (e.g., radial basis functions) to capture local geometric structure. When label information is available, however, meaningful representations should reflect not only feature–feature relationships but also feature–label dependencies. In such settings, purely unsupervised geometry can be misleading, as it treats all features equally regardless of their relevance to the label signal.

Pairwise proximities derived from leaf co-occurrence in trained Random Forests (RFs) or other tree ensembles (Breiman, 2001; Breiman & Cutler, 2003; Tan et al., 2020; Rhodes et al., 2023b) address this limitation by jointly capturing similarity in the feature space and the task-relevant structure, implicitly downweighting features that are irrelevant for prediction. In particular, RF-GAP proximities (Rhodes et al., 2023b) provide a robust label-informed proximity measure through a leaf weighting scheme based on in-bag/out-of-bag status, which reflects the predictive behavior of the underlying forest. This property has led to substantial improvements in guided representation learning compared to standard forest-based proximity definitions and Euclidean class-conditional approaches (Rhodes et al., 2023a; Aumon et al., 2025). In addition, tree-induced proximities naturally accommodate both continuous and categorical features and scale near-linearly in time and memory (Aumon et al., 2026), whereas Euclidean kernels rely on quadratic pairwise distance computations and often require approximate nearest-neighbor methods to remain tractable (Indyk & Motwani, 1998).

2.2. Manifold alignment approaches

Given multiple domains containing observations from different modalities that describe related phenomena, manifold alignment (MA) aims to learn a shared representation that preserves both (i) the intrinsic geometric structure within each domain and (ii) information shared across domains. While intra-domain geometry can typically be inferred directly from the respective feature spaces, capturing shared cross-domain information depends critically on the assump-

tions made about how the domains are related.

Semi-supervised MA assumes access to a subset of one-to-one correspondences across domains, which serve as anchor points to guide alignment. These anchors provide explicit cross-domain constraints that allow the remaining unmatched samples to be embedded into a common space.

Traditional approaches include canonical correlation analysis (Thompson, 1984), which learns linear projections that maximize the correlation between paired observations. While efficient, such global linear models are often inadequate for capturing the nonlinear structure of high-dimensional data. This limitation motivated subsequent graph-based methods (Ham et al., 2003; 2005), which preserve local manifold geometry within each domain while enforcing alignment through anchor constraints. Alternatively, Wang & Mahadevan (2008) projects both domains into a shared space using dimensionality reduction (DR), followed by Procrustes alignment on anchor points, and generally outperforms earlier approaches.

More recent semi-supervised MA methods leverage anchor correspondences while better preserving intra-domain geometry. Generative approaches (Amodio & Krishnaswamy, 2018) learn mappings between domains in a CycleGAN-style framework (Zhu et al., 2017), augmented with correspondence losses to enforce alignment consistency and reduce superimposition. Duque et al. (2023b) incorporates diffusion geometry by using anchor correspondences to derive diffusion-informed inter-domain distances, which define the cost of an entropic OT problem (Peyré et al., 2019); the resulting coupling is then used to construct inter-domain affinities prior to joint embedding. In contrast, Rhodes & Rustad (2024a) aligns domains by directly linking their diffusion operators through a union graph. Building on this idea, Rhodes & Rustad (2024b) moves beyond Euclidean-based alignment by using RF-derived affinities within each domain. However, their method assumes fully labeled source and target domains, which could be restrictive; we relax this assumption in Section 3.2 by allowing partially labeled settings.

Anchor-based approaches rely on known correspondences, which can be expensive or impossible to obtain. This limitation is particularly pronounced in biological applications, where measurement processes are often destructive and prevent observing multiple modalities from the same cells.

Unsupervised MA is the most challenging setting, as it assumes no explicit shared information across domains. However, domains describing the same phenomenon are expected to exhibit similar underlying structure. This assumption allows correspondences to be inferred indirectly by relating points across domains based solely on their locations within their respective manifolds.

Early unsupervised approaches sought to recover shared

structure by constructing joint representations from intra-domain geometry. Wang & Mahadevan (2009) introduced a cross-domain heat kernel based on permutations of local geometric structure, combined with intra-domain kernels, followed by DR to obtain a shared embedding. Subsequent work framed unsupervised MA as a problem of implicit global distribution matching, e.g., by minimizing discrepancies between kernel mean embeddings (Liu et al., 2019) or by matching intrinsic geometric structure using geodesic distances rather than kernel matrices (Cao et al., 2020).

Rather than enforcing global matching, a complementary line of work infers correspondences through local neighborhood consistency. Haghverdi et al. (2018) and Hie et al. (2019) identify mutual nearest neighbors across domains and use these pairs as anchors to apply local, translation-based corrections. Similarly, Korsunsky et al. (2019) and Welch et al. (2019) rely on local alignment heuristics, using cluster-wise linear corrections or shared (dataset-invariant) latent factors, respectively.

To move beyond heuristic local matching and explicitly enforcing global geometric consistency, another line of work formulates unsupervised MA as an OT problem. In this setting, correspondences are inferred globally using the Gromov–Wasserstein OT family (GWOT; (Mémoli, 2011)), with discrepancies in geodesic distances serving as the transport cost, followed by DR (Demetci et al., 2022; Cao et al., 2021). Alternatively, Chen et al. (2022) extends Procrustes-based alignment by first projecting each domain into a shared latent space and then refining the alignment via Wasserstein Procrustes (Grave et al., 2019).

Even in the absence of explicit correspondences, one does not need to resort to fully unsupervised manifold alignment when side information is available in both domains.

Label-supervised MA occupies a middle ground between fully unsupervised and semi-supervised MA by leveraging an auxiliary form of shared information. A common source of such side information is a set of discrete class labels (Wang & Mahadevan, 2011; Tuia & Camps-Valls, 2016; Wang et al., 2019), for example, known cell types between batches in single-cell analysis (Cao et al., 2021).

Early work in this setting directly learned a latent joint representation by incorporating label information into the alignment objective, enforcing strict same-class matching alongside intra-domain geometric regularization (Wang & Mahadevan, 2011; Tuia & Camps-Valls, 2016). However, this strategy is highly sensitive to label availability, as samples with missing labels are left unmatched. In contrast, Manifold Alignment with Label Information (MALI; Duque et al. (2023a)) adopts a two-stage approach in which cross-domain correspondences are first inferred through an OT formulation, and a joint similarity matrix is then constructed

from the resulting coupling. This matrix can subsequently be used to obtain a shared latent representation if desired. MALI proceeds similarly to Duque et al. (2023b), but replaces cross-domain diffusion-based distances through anchors with cosine distances between semantic representations, defined as projections onto a label space obtained by aggregating class-wise affinities within each domain.

In single-cell analysis, recent methods extend unsupervised GWOT alignment by incorporating labels into the transport cost, thus favoring matches between cells of the same type (Cao et al., 2021). Others leverage label information through probabilistic deep generative models for batch correction (Xu et al., 2021). However, these generative models typically assume that all domains share the same feature space, limiting them to homogeneous data integration

These methods fall under a *weakly* supervised MA setting, as correspondences are inferred rather than provided explicitly, while still exploiting shared semantic information across domains. Although more effective than purely unsupervised approaches, existing methods in this category continue to rely on unsupervised, Euclidean-based intra-domain geometry, overlooking the available label information. Moreover, MALI relies on diffusion pseudotime (DPT; Haghverdi et al. (2016)) and explicit OT, leading to polynomial time and memory complexity. In this work, we explore the benefits of leveraging forest-induced intra- and cross-domain geometry for manifold alignment in the weakly supervised setting, while maintaining high scalability.

3. Methods

3.1. Problem formulation

Given a source domain $\mathcal{X}_A = \{\mathbf{x}_1^A, \dots, \mathbf{x}_n^A\}$ and a target domain $\mathcal{X}_B = \{\mathbf{x}_1^B, \dots, \mathbf{x}_m^B\}$, manifold alignment aims to learn a shared representation that preserves both intra-domain geometric structure and cross-domain relationships.

We consider a weakly supervised setting in which the two domains share a common label space, but explicit correspondences are unavailable. We further relax the fully labeled assumption by allowing one domain—typically the target domain—to be only partially labeled. Let $\mathcal{Y}_A = \{\mathbf{y}_1^A, \dots, \mathbf{y}_n^A\}$ and $\mathcal{Y}_B = \{\mathbf{y}_1^B, \dots, \mathbf{y}_r^B\}$, with $r \leq m$, denote the observed labels in the source and target domains, respectively. We assume that labels take values in a shared finite class set $\mathcal{C} = \{1, \dots, C\}$, and that each class $c \in \mathcal{C}$ is represented by at least one sample in each domain. The goal is therefore to leverage this limited shared supervision to infer meaningful relationships across domains.

Our method focuses on learning cross-domain similarities that are comparable in scale to intra-domain affinities, which naturally supports both correspondence estimation and the

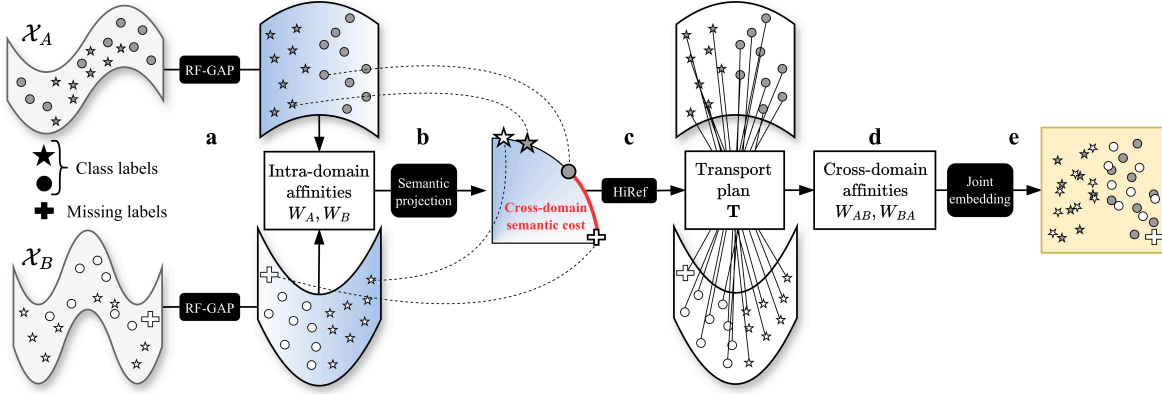


Figure 1. Overview of FoSTA. **(a)** Given two (partially labeled) domains \mathcal{X}_A and \mathcal{X}_B , we compute semi-supervised, label-informed RF-GAP intra-domain affinities W_A and W_B to capture task-relevant neighborhood structure (Section 3.2). **(b)** We form class-wise semantic profiles and map samples from both domains to a shared, ℓ_2 -normalized semantic space, which defines a cross-domain semantic cost (Section 3.3). **(c)** Using this cost, HiRef estimates an efficient bijective transport plan \mathbf{T} between domains (Section 3.3). **(d)** We propagate correspondences through \mathbf{T} to build cross-domain affinities W_{AB} and W_{BA} consistent with the intra-domain graphs (Section 3.4). **(e)** Finally, we compute a joint low-dimensional embedding from the resulting block affinity matrix (Section 3.5).

construction of shared embeddings (Duque et al., 2023b;a). Thus, the core objective is to build a joint affinity matrix of the form

$$\mathbf{W} = \begin{bmatrix} W_A & W_{AB} \\ W_{BA} & W_B \end{bmatrix} \in \mathbb{R}_{\geq 0}^{(n+m) \times (n+m)},$$

where the diagonal blocks represent intra-domain affinities and the off-diagonal blocks represent cross-domain affinities. The construction of each affinity block is detailed in the sections that follow, and Fig. 1 presents a schematic representation of our FoSTA framework.

3.2. Label-informed intra-domain affinities

For clarity, we focus on the balanced case $n = m$. Extensions to imbalanced settings are discussed in Appendix D. Let $\mathcal{X}_* = \{\mathbf{x}_1^*, \dots, \mathbf{x}_n^*\}$ denote a partially labeled domain, with $* \in \{A, B\}$. We partition the index set as $\mathcal{I}_*^l = \{i : \mathbf{x}_i^* \text{ is labeled}\}$ and $\mathcal{I}_*^u = \{i : \mathbf{x}_i^* \text{ is unlabeled}\}$, with $\mathcal{I}_*^l \cup \mathcal{I}_*^u = \{1, \dots, n\}$. Our goal is to construct class-aware intra-domain affinities that better capture the structure of \mathcal{X}_* relative to the class labels than standard Euclidean kernels. We build on the RF-GAP proximity (Rhodes et al., 2023b), augmented with self-similarity (Rhodes et al., 2023a; Aumon et al., 2025). Let a random forest (RF) be trained on the labeled samples $\{\mathbf{x}_j^* : j \in \mathcal{I}_*^l\}$. For any query index $i \in \{1, \dots, n\}$ and labeled target index $j \in \mathcal{I}_*^l$, the directed RF-GAP proximity is defined as

$$p_l^*(\mathbf{x}_i^*, \mathbf{x}_j^*) = \begin{cases} \frac{1}{|S_i^*|} \sum_{t \in S_i^*} \frac{c_j^*(t) I(\ell_i^*(t) = \ell_j^*(t))}{|M_i^*(t)|}, & i \neq j, \\ \frac{1}{|\bar{S}_i^*|} \sum_{t \in \bar{S}_i^*} \frac{c_i^*(t)}{|M_i^*(t)|}, & i = j, \end{cases}$$

where S_i^* (\bar{S}_i^*) denotes the set of out-of-bag (in-bag) trees for \mathbf{x}_i^* , $c_j^*(t)$ is the in-bag multiplicity of \mathbf{x}_j^* in tree t , $\ell_i^*(t)$ is the terminal leaf of \mathbf{x}_i^* , and $M_i^*(t)$ is the multiset of in-bag samples in that leaf. This formulation naturally applies to both labeled-labeled and unlabeled-labeled interactions, since unlabeled samples are out-of-bag for all trees (Aumon et al., 2025). Because RF-GAP proximities are generally asymmetric, we symmetrize them using $(W_*^l)_{ij} = \frac{1}{2} [p_l^*(\mathbf{x}_i^*, \mathbf{x}_j^*) + p_l^*(\mathbf{x}_j^*, \mathbf{x}_i^*)]$, for $i, j \in \mathcal{I}_*^l$. This symmetrization facilitates downstream methods that require symmetric affinities and aligns the labeled proximities with the extensions introduced below.

The original RF-GAP does not define proximities when the target sample is unlabeled, as such points lack in-bag status. To extend the definition, we model unlabeled samples using their expected bootstrap behavior (Breiman, 1996). In expectation, each training sample has unit in-bag multiplicity and is covered by all T_* trees. We therefore treat unlabeled samples as *pseudo-training* points with unit in-bag weight ($c_j^*(t) = 1$) and full expected coverage across the forest. Accordingly, unlabeled samples act as out-of-bag queries, while contributing as unit-weight in-bag targets. Under this assumption, for any query index $i \in \{1, \dots, n\}$ and unlabeled target index $j \in \mathcal{I}_*^u$, we define

$$p_u^*(\mathbf{x}_i^*, \mathbf{x}_j^*) = \frac{1}{|S_i^*|} \sum_{t \in S_i^*} \frac{I(\ell_i^*(t) = \ell_j^*(t))}{|M_i^*(t)|}.$$

This extension preserves the RF-GAP principle of leaf co-occurrence normalized by leaf size and ensures scale compatibility with p_l^* . We set the remaining affinity blocks to

$$(W_*^{ul})_{ij} = \frac{1}{2} [p_l^*(\mathbf{x}_i^*, \mathbf{x}_j^*) + p_u^*(\mathbf{x}_j^*, \mathbf{x}_i^*)],$$

$$(W_*^{uu})_{ij} = p_u^*(\mathbf{x}_i^*, \mathbf{x}_j^*),$$

for $(i, j) \in (\mathcal{I}_*^u, \mathcal{I}_*^l)$ and $i, j \in \mathcal{I}_*^u$, respectively. With $W_*^{lu} = (W_*^{ul})^\top$, the full intra-domain affinity matrix is

$$W_* = \begin{bmatrix} W_*^{ll} & W_*^{lu} \\ W_*^{ul} & W_*^{uu} \end{bmatrix} \in \mathbb{R}_{\geq 0}^{n \times n}. \quad (1)$$

3.3. Learning correspondences via semantic transport

To establish correspondences across domains, we seek a shared representation that abstracts away domain-specific variability while preserving class-level structure. Starting from the label-informed RF-GAP affinity matrix W_* (Eq. 1), we construct a *semantic profile* for each sample that summarizes its relationships to labeled data across classes.

Specifically, for any point $\mathbf{x}_i \in \mathcal{X}_*$, we define a C -dimensional semantic vector

$$S_*(i, c) = \frac{1}{p_c^*} \sum_{j \in \mathcal{I}_*^c} (W_*)_{ij},$$

where \mathcal{I}_*^c denotes the set of samples in domain $*$ labeled with class c , and $p_c^* = |\mathcal{I}_*^c|/|\mathcal{I}_*^l|$ is the estimated prior probability of that class. The normalization by $1/p_c^*$ mitigates class imbalance, ensuring that rare and frequent classes contribute comparably to the semantic representation. Each sample is thus embedded into a shared semantic space, regardless of its original domain. Intuitively, samples with similar semantic roles (e.g., strong affinity to one class and weak affinity to others) are mapped close to each other, while samples associated with different classes are separated. Unlike MALI, which relies on expensive DPT to produce coarse semantic representations, we derive them directly from the affinity matrix.

Before alignment, we ℓ_2 -normalize these semantic vectors,

$$\tilde{S}_*(i, \cdot) = \frac{S_*(i, \cdot)}{\|S_*(i, \cdot)\|_2}, \quad (2)$$

which enforces scale invariance and ensures that alignment depends only on the relative shape of the class-affinity profiles. This normalization also enables efficient downstream optimization, as discussed below.

To align samples across domains, one could naively rely on a cross-domain k -nearest neighbors graph. However, formulating alignment as an OT assignment has been shown to provide greater robustness by enforcing global structural consistency across domains (Duque et al., 2023b;a). Given normalized semantic representations $\tilde{S}_A, \tilde{S}_B \in \mathbb{R}^{n \times C}$, we define the OT problem

$$\mathbf{T}^* = \arg \min_{\mathbf{T} \in \mathcal{U}} \langle \mathbf{T}, \mathbf{C} \rangle,$$

where $\mathbf{C}_{ij} = \|\tilde{S}_A(i, \cdot) - \tilde{S}_B(j, \cdot)\|_2^2$ is the pairwise cost matrix, $\langle \cdot, \cdot \rangle$ denotes the Frobenius inner product, and

$$\mathcal{U} = \{ \mathbf{T} \in \{0, 1\}^{n \times n} \mid \mathbf{T}\mathbf{1} = \mathbf{1}, \mathbf{T}^\top \mathbf{1} = \mathbf{1} \}$$

is the set of bijective couplings. The optimal coupling \mathbf{T}^* defines a one-to-one correspondence between samples in the two domains.

Solving this OT problem exactly is computationally prohibitive for large-scale datasets, as it requires explicit construction of the dense cost matrix \mathbf{C} , leading to at least quadratic time and memory complexity. We therefore approximate \mathbf{T}^* using HiRef (Halmos et al., 2025), which recursively partitions the source and target domains and solves a sequence of smaller, localized transport problems. This divide-and-conquer strategy yields quasilinear complexity while producing a sparse, bijective Monge map.

Finally, note that on the unit hypersphere induced by ℓ_2 normalization in Eq. 2, minimizing squared Euclidean distance is equivalent to maximizing cosine similarity. This equivalence allows HiRef to leverage fast low-rank factorizations of the Euclidean cost (Scetbon et al., 2021) without explicitly forming \mathbf{C} , effectively performing cosine-based semantic matching while retaining the scalability of the Euclidean-based HiRef solver. The resulting coupling $\mathbf{T} \approx \mathbf{T}^*$ thus provides an efficient and robust cross-domain correspondence.

3.4. Cross-domain affinities through correspondence propagation

While one could directly populate the off-diagonal blocks of the joint affinity matrix using the binary assignment encoded by \mathbf{T} (i.e., setting entries to either 0 or 1), such a construction fails to capture meaningful similarities between pairs that are not directly matched. I.e., it provides no notion of graded cross-domain similarity beyond the hard assignment.

To obtain smoother and more informative cross-domain affinities, we propagate intra-domain affinities across the estimated correspondences by transferring local geometric structure from each domain to the other:

$$W_{AB} = \frac{1}{2} [W_A \mathbf{T} + \mathbf{T} W_B], \quad W_{BA} = W_{AB}^\top.$$

As a result, two samples from different domains are assigned a high affinity if they are either directly matched by \mathbf{T} or if they are close to matched samples within their respective domains. This construction yields cross-domain similarities that are consistent in scale with intra-domain affinities and better reflect the underlying manifold structure across domains.

3.5. Joint embedding

The final step of our framework projects both domains into a shared latent space. Given the label-informed cross-domain affinities, a natural approach would be to perform a barycentric projection, i.e., to map samples from one domain onto the other using weighted averages of neighboring coordinates. However, such projections are highly sensitive to the curse of dimensionality and operate directly in the original feature space. This is undesirable in our setting, as the raw feature space may be noisy and may not faithfully reflect the underlying phenomenon of interest.

Instead, we rely on nonlinear, kernel-based DR to embed both domains into a shared low-dimensional representation. Specifically, we use Landmark PHATE (Moon et al., 2019), a scalable variant of PHATE, which has been shown to work effectively with forest-derived affinities in guided representation learning (Rhodes et al., 2023a; Aumon et al., 2025).

3.6. Complexity analysis

One of FoSTA’s key strengths is its scalability, making it well-suited for large-scale data integration. This stems from the natural sparsity of the leaf-based RF-GAP affinity construction, combined with fast hierarchical OT and Landmark PHATE embeddings that avoid full kernel diffusion. Together, these components yield log-linear time complexity and linear memory complexity in the number of samples. In contrast, MALI and related OT-based MA methods typically require at least quadratic time and space. A detailed complexity analysis is provided in Appendix A.

4. Empirical Results

4.1. Multimodal alignment for data integration

We compared FoSTA with four weakly supervised manifold alignment baseline methods that also exploit label information: kernel manifold alignment with radial basis function (KEMArbf; Tuia & Camps-Valls (2016)) and its linear variant (KEMAlin; Wang & Mahadevan (2011)), MALI (Duque et al., 2023a), and Pamona (Cao et al., 2021) with label-informed cost correction. Since we assume full overlap between domains, we remove the virtual cells from the GWOT formulation in Pamona, ensuring a fair comparison.

Using 15 supervised learning datasets from the [UCI Machine Learning Repository](#) (Kelly, Longjohn & Nottingham; see Appendix B), we apply different methods to artificially split the data into two domains (Rhodes & Rustad, 2024b). The *random* split randomly assigns features to either domain. The *importance* split assigns the most task-relevant features, as classified by a random forest model, to the first domain, and the least important features to the second domain. The *alternating importance* split assigns features to

Table 1. Aggregated performance over 15 UCI datasets under different distortion splits. Results are reported for label transfer accuracy, alignment score (AS), and correspondence recovery measured by FOSCTTM. Higher values indicate better performance for accuracy and AS, while lower ones indicate better performance for FOSCTTM. FoSTA achieves superior accuracy in all cases, and superior FOSCTTM in all but one, compared to other methods. In terms of AS, FoSTA is either 2nd or 3rd. As explained in Section 4.1, we prioritize accuracy and FOSCTTM over AS.

Split	Model	Accuracy \uparrow	AS \uparrow	FOSCTTM \downarrow
add noise features	FoSTA	0.766	0.388	0.223
	KEMAlin	0.595	0.001	0.443
	KEMArbf	0.513	0.018	0.444
	MALI	<u>0.713</u>	0.933	<u>0.340</u>
alternating importance	Pamona	<u>0.639</u>	<u>0.718</u>	<u>0.430</u>
	FoSTA	0.772	<u>0.720</u>	0.313
	KEMAlin	0.481	0.035	0.461
	KEMArbf	0.508	0.030	0.462
distort	MALI	<u>0.637</u>	0.982	<u>0.375</u>
	Pamona	<u>0.634</u>	<u>0.490</u>	<u>0.394</u>
	FoSTA	0.782	0.757	0.216
	KEMAlin	0.588	0.021	0.444
importance	KEMArbf	0.541	0.030	0.453
	MALI	<u>0.726</u>	0.980	<u>0.256</u>
	Pamona	<u>0.678</u>	<u>0.766</u>	<u>0.256</u>
	FoSTA	0.789	<u>0.643</u>	0.305
random	KEMAlin	0.499	0.028	0.452
	KEMArbf	0.489	0.051	0.458
	MALI	<u>0.631</u>	0.947	<u>0.389</u>
	Pamona	<u>0.717</u>	<u>0.481</u>	<u>0.382</u>
rotate	FoSTA	0.747	<u>0.669</u>	0.326
	KEMAlin	0.601	0.061	0.449
	KEMArbf	0.498	0.028	0.465
	MALI	<u>0.604</u>	0.978	<u>0.377</u>
rotate	Pamona	<u>0.637</u>	<u>0.466</u>	<u>0.400</u>
	FoSTA	0.809	0.754	0.207
	KEMAlin	0.599	0.054	0.431
	KEMArbf	0.467	0.047	0.446
rotate	MALI	<u>0.734</u>	1.010	<u>0.197</u>
	Pamona	<u>0.756</u>	<u>1.002</u>	0.100

either domain by alternating by feature importance, creating balanced domains. In the *add noise* split, both domains contain all of the features, but the second additionally contains noise features, with a signal-to-noise ratio of 1 to 10. As baselines, we also consider the *distort* split, which creates a second domain by adding Gaussian noise to the first, and the *rotate* split, which creates a second domain by a random rotation of the first. For robustness, we use 5 different random seeds to generate the domains and report the averages. We masked 50% of the target labels to evaluate models in semi-supervised settings.

We evaluate the models on three complementary tasks: label transfer, domain mixing, and correspondence recovery. Label transfer accuracy is measured by predicting masked target labels using a k -nearest neighbors classifier trained

on the source embeddings (Cao et al., 2020; Demetci et al., 2022). Domain mixing is quantified by an alignment score (AS; Butler et al. (2018)) defined as $2(1 - \bar{k}/k)$, where \bar{k} is the average number of k -nearest neighbors belonging to the same domain as the query sample. An AS near 1 indicates perfect mixing, while 0 indicates complete separation. Correspondence recovery is assessed using the Fraction of Samples Closer Than the True Match (FOSCTTM; Liu et al. (2019)), which measures the proportion of cross-domain neighborhoods that exclude the true match (lower is better).

FoSTA consistently achieves the highest label transfer accuracy and the lowest FOSCTTM in nearly all settings, with the exception of the rotation split (see Table 1). FoSTA is also either second or third best in AS. These results indicate that FoSTA more reliably recovers meaningful cross-domain correspondences and preserves task-relevant semantic structure compared to competing methods. We emphasize label transfer accuracy and correspondence recovery over the AS, as these metrics are directly grounded in available ground-truth information. Label transfer evaluates whether semantic information is preserved across domains, while FOSCTTM explicitly measures the recovery of true cross-domain correspondences. In contrast, the AS is a heuristic that assesses domain mixing under the assumption that local neighborhoods should contain uniformly distributed samples from each domain. As a result, a method could achieve a high AS by indiscriminately mixing domains—potentially even collapsing structure—without accurately aligning shared semantic manifolds. That is, a moderate AS does not contradict strong performance in label transfer and correspondence recovery, which provide a more faithful assessment of alignment quality in our setting.

4.2. Batch effect removal in single-cell genomics

We now consider the task of batch effect removal in single-cell genomics, where the goal is to combine data batches of a single modality (i.e., sharing the same feature space). Different batches may contain data collection artifacts called batch effects, which are due to a different environment or setup (e.g., the used protocol, time, instrument, or donors) when collecting the data. Batch effects are widespread in single-cell data, and must be removed so that downstream analyses are not impacted by them (Haghverdi et al., 2018; Stuart et al., 2019; Tran et al., 2020; Luecken et al., 2022; Leek et al., 2010).

We simulate batches by adding different noise and dropout levels to real single-cell RNA-seq data. We use the lung atlas dataset from (Vieira Braga et al., 2019), which we access via the scib-metrics package (Luecken et al., 2022) and subset to the largest existing batch (batch 4). To quantitatively evaluate a method’s ability to correct the batch effects while retaining underlying biological patterns, we

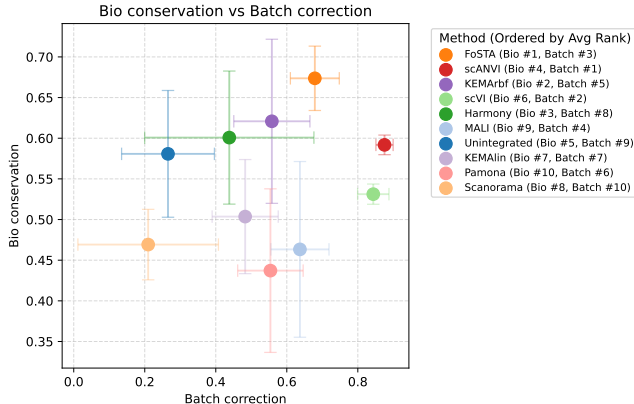


Figure 2. Biological preservation (bio) vs. batch correction (batch) scores (Luecken et al., 2022) for simulated batch effect removal on lung single-cell data (Vieira Braga et al., 2019). The legend is ordered according to average method ranks in these two aspects, with FoSTA leading the average ranking (as 1st in bio and 3rd in batch) followed by scANVI (1st in batch but 4th in bio) and others.

follow the extensive benchmark suggested by Luecken et al. (2022) and use a set of twelve metrics: seven that evaluate biological conservation and five that evaluate batch correction (see Appendix C for metric details). We note that these metrics differ from those used in Section 4.1, since in this case there are no true correspondences between batches.

To simulate a range of batch correction scenarios, we randomly split the samples of the dataset into two simulated batches, and apply Gaussian noise and dropout (i.e., randomly masking elements of the input matrix with probability p) to the second batch. The standard deviation of the Gaussian noise is varied between 0 and 1 in regular intervals of 0.1. Similarly, the dropout probability is varied in regular intervals of 0.1 between 0 and 0.9.

We consider all combinations of noise and dropout, yielding a total of 110 experimental scenarios. In each scenario, datasets are integrated and embedded using FoSTA and eight prominent batch correction methods. These include Scanorama (Hie et al., 2019) and Harmony (Korsunsky et al., 2019), which are unsupervised methods relying on local anchoring strategies; scVI and its label-supervised variant scANVI (Xu et al., 2021), which are probabilistic deep generative models; MALI (Duque et al., 2023a) and Pamona (Cao et al., 2021), which are label-supervised OT-based methods; and both linear and RBF variants of KEMA (Wang & Mahadevan, 2011; Tuia & Camps-Valls, 2016), which are label-supervised kernel-based approaches.

Since we focus on the task of joint visualization, we require all methods to produce 2-dimensional embeddings. Aggregate scores are computed by averaging the seven biological conservation metrics and averaging the five batch correction metrics from Luecken et al. (2022). These are then com-

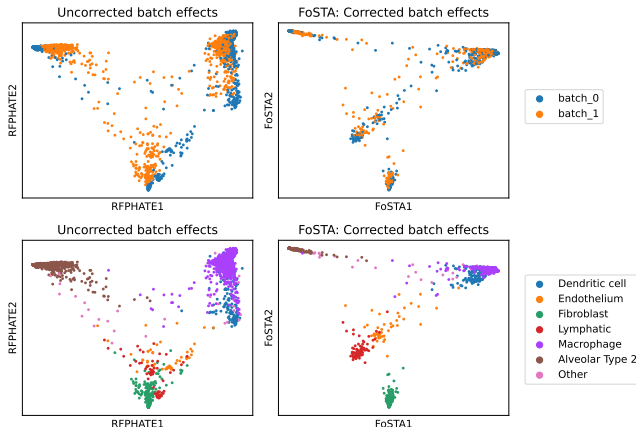


Figure 3. Embeddings of the simulated batch integration task. Left column: data before correcting for batch effects, visualized with RF-PHATE (Rhodes et al., 2023a) supervised by cell type labels. Right column: resulting embedding after applying FoSTA to correct the batch effects. The plots are colored by simulated batch (top), and cell type (bottom). FoSTA mixes the batches well, while preserving the biological structure of the data.

puted and averaged over the 110 simulated batch-correction scenarios, with the resulting balance between the two aspects, for each method, shown in Figure 2. Scores for the individual metrics are given in Appendix E.

As discussed in Luecken et al. (2022), some tradeoff is expected between biological conservation and batch correction, with methods that emphasize removal of strong batch effects often sacrificing some underlying meaningful variance that is inadvertently correlated with variation between batches. Due to the annotation guidance incorporated in FoSTA, we expect it to lean more towards the conservation aspect. Indeed, as shown in Figure 2, FoSTA outperforms all other methods in biological conservation while still demonstrating a reasonably high batch conservation score, above all but two competitors. While scANVI and scVI achieve higher batch correction scores, their biological conservation is substantially lower (ranked third and sixth, respectively). Further, we note that batch correction metrics essentially quantify the mixing (or inseparability) between batches, which could be trivially achieved in various naïve ways (e.g., collapsing all variability in the data or projecting on directions of least variance between batches) without retaining any informative structure. Therefore we argue that they should be considered secondary to the biological conservation ones, i.e., serving to verify mitigation of batch effects but subject to the retention of biological information. Therefore, with this perspective, our results in Fig. 2 demonstrate that we achieve a good balance between the two sets of metrics.

To further demonstrate the use of FoSTA for data exploration under batch-effect conditions, Fig. 3 shows its em-

bedding of the lung data from two batches, under moderate amount of noise and dropout (both set to 0.5) on one of the batches. The uncorrected plots clearly show that the batch effects and noise distort the embedding (e.g., mixing endothelium, lymphatic, and fibroblast cells) while the FoSTA plots show that we are able to correct them. We can clearly identify prominent cell types in the lungs in the FoSTA plots, as well as potential connections between them that are consistent with known biology. These include the proximity between dendritic cells and macrophages, which commonly work together to maintain the immune system of the lungs (Guilliams et al., 2013), as well as potential communication pathways between Alveolar Type 2 cells and macrophages, which is critical for lung function and development (Gschwend et al., 2021; Clements & Idoyaga, 2021). The proximity between endothelium and lymphatic endothelial cells (while still being clearly distinguishable) also corresponds well to their transcriptomic similarity, as well as their positioning with respect to fibroblast cells, potentially reflecting known interaction between these cell populations (Vieira Braga et al., 2019).

5. Conclusion and discussion

We proposed FoSTA, a forest-guided framework for label-supervised manifold alignment that replaces Euclidean intra-domain geometry with task-adaptive, label-informed forest affinities and performs scalable semantic optimal transport for cross-domain matching. By separating geometry learning, correspondence estimation, and embedding construction, FoSTA offers a flexible computationally-efficient alternative to existing weakly supervised alignment methods.

On synthetic multimodal integration benchmarks, FoSTA consistently improves label transfer accuracy and correspondence recovery compared to established baselines. On single-cell data it achieves strong biological preservation across a wide range of simulated batch effects, while remaining competitive in batch correction. Although performance on certain batch correction or alignment metrics may seem degraded, such metrics can be misleading, as they do not necessarily reflect correspondence quality or downstream performance. These results support our central hypothesis that forest-induced geometry better captures task-relevant structure than Euclidean kernels.

Conceptually, FoSTA differs from prior label-supervised alignment methods by avoiding diffusion-based preprocessing and dense OT, yielding near-linear scaling in the number of samples. The proposed semi-supervised extension of RF-GAP proximities further enables unlabeled samples to contribute meaningfully to the learned geometry, which is critical in realistic partially labeled settings. Limitations include the assumption of shared label sets across domains and dependence on the quality of the underlying forest

model. Extending FoSTA to partially overlapping label spaces, softer correspondence models, or alternative transport formulations remains an important direction for future work. Overall, our results highlight the importance of task-aware geometry in weakly supervised manifold alignment and demonstrate that tree-based representations provide a scalable and effective foundation for this setting.

Impact Statement

This paper presents work whose goal is to advance the field of Machine Learning. There are many potential societal consequences of our work, none which we feel must be specifically highlighted here.

References

- Amodio, M. and Krishnaswamy, S. MAGAN: Aligning Biological Manifolds. In *Proceedings of the 35th International Conference on Machine Learning*, pp. 215–223. PMLR, July 2018.
- Aumon, A., Ni, S., Lizotte, M., Wolf, G., Moon, K. R., and Rhodes, J. S. Random Forest Autoencoders for Guided Representation Learning. In *The Thirty-ninth Annual Conference on Neural Information Processing Systems*, October 2025.
- Aumon, A., Wolf, G., Moon, K. R., and Rhodes, J. S. Scalable Tree Ensemble Proximities in Python. *arXiv preprint arXiv:2601.02735*, 2026.
- Breiman, L. Bagging predictors. *Machine learning*, 24(2): 123–140, 1996.
- Breiman, L. Random Forests. *Machine Learning*, 45(1): 5–32, October 2001. ISSN 1573-0565. doi: 10.1023/A:1010933404324.
- Breiman, L. and Cutler, A. Manual on setting up, using, and understanding random forests v4.0. Technical report, University of California, Berkeley, Department of Statistics, 2003.
- Butler, A., Hoffman, P., Smibert, P., Papalexi, E., and Satija, R. Integrating single-cell transcriptomic data across different conditions, technologies, and species. *Nature biotechnology*, 36(5):411–420, 2018.
- Büttner, M., Miao, Z., Wolf, F. A., Teichmann, S. A., and Theis, F. J. A test metric for assessing single-cell rna-seq batch correction. *Nature methods*, 16: 43–49, 1 2019. ISSN 1548-7105. doi: 10.1038/S41592-018-0254-1. URL <https://pubmed.ncbi.nlm.nih.gov/30573817/>.
- Caffarelli, L. A. and McCann, R. J. Free boundaries in optimal transport and Monge-Ampere obstacle problems. *Annals of mathematics*, pp. 673–730, 2010.
- Cao, K., Bai, X., Hong, Y., and Wan, L. Unsupervised topological alignment for single-cell multi-omics integration. *Bioinformatics*, 36(Supplement_1):i48–i56, July 2020. ISSN 1367-4803. doi: 10.1093/bioinformatics/btaa443.
- Cao, K., Hong, Y., and Wan, L. Manifold alignment for heterogeneous single-cell multi-omics data integration using Pamona. *Bioinformatics*, 38(1):211–219, December 2021. ISSN 1367-4803. doi: 10.1093/bioinformatics/btab594.
- Chapel, L., Alaya, M. Z., and Gasso, G. Partial optimal transport with applications on positive-unlabeled learning. *Advances in Neural Information Processing Systems*, 33: 2903–2913, 2020.
- Chawla, N. V., Bowyer, K. W., Hall, L. O., and Kegelmeyer, W. P. SMOTE: Synthetic minority over-sampling technique. *Journal of artificial intelligence research*, 16: 321–357, 2002.
- Chen, D., Fan, B., Oliver, C., and Borgwardt, K. Unsupervised Manifold Alignment with Joint Multidimensional Scaling. In *The Eleventh International Conference on Learning Representations*, September 2022.
- Clements, D. and Idoyaga, J. Alveolar macrophages and epithelial cells: The art of living together. *The Journal of Experimental Medicine*, 218(10):e20211583, 2021.
- Danon, L., Díaz-Guilera, A., Duch, J., and Arenas, A. Comparing community structure identification. *Journal of Statistical Mechanics: Theory and Experiment*, 2005:P09008, 9 2005. ISSN 1742-5468. doi: 10.1088/1742-5468/2005/09/P09008. URL <https://iopscience.iop.org/article/10.1088/1742-5468/2005/09/P09008https://iopscience.iop.org/article/10.1088/1742-5468/2005/09/P09008/meta>.
- Demaine, E., Hesterberg, A., Koehler, F., Lynch, J., and Urschel, J. Multidimensional Scaling: Approximation and Complexity. In *Proceedings of the 38th International Conference on Machine Learning*, pp. 2568–2578. PMLR, July 2021.
- Demetci, P., Santorella, R., Sandstede, B., Noble, W. S., and Singh, R. SCOT: Single-cell multi-omics alignment with optimal transport. *Journal of computational biology*, 29(1):3–18, 2022.

- Duque, A. F., Lizotte, M., Wolf, G., and Moon, K. R. Manifold Alignment with Label Information. In *2023 International Conference on Sampling Theory and Applications (SampTA)*, pp. 1–6, July 2023a. doi: 10.1109/SampTA59647.2023.10301369.
- Duque, A. F., Wolf, G., and Moon, K. R. Diffusion Transport Alignment. In Crémilleux, B., Hess, S., and Nijssen, S. (eds.), *Advances in Intelligent Data Analysis XXI*, pp. 116–129, Cham, 2023b. Springer Nature Switzerland. ISBN 978-3-031-30047-9. doi: 10.1007/978-3-031-30047-9_10.
- Grave, E., Joulin, A., and Berthet, Q. Unsupervised Alignment of Embeddings with Wasserstein Procrustes. In *Proceedings of the Twenty-Second International Conference on Artificial Intelligence and Statistics*, pp. 1880–1890. PMLR, April 2019.
- Gschwend, J., Sherman, S. P., Ridder, F., Feng, X., Liang, H.-E., Locksley, R. M., Becher, B., and Schneider, C. Alveolar macrophages rely on GM-CSF from alveolar epithelial type 2 cells before and after birth. *Journal of Experimental Medicine*, 218(10):e20210745, 2021.
- Guilliams, M., Lambrecht, B.N., and Hammad, H. Division of labor between lung dendritic cells and macrophages in the defense against pulmonary infections. *Mucosal immunology*, 6(3):464–473, 2013.
- Haghverdi, L., Büttner, M., Wolf, F. A., Büttner, F., and Theis, F. J. Diffusion pseudotime robustly reconstructs lineage branching. *Nature methods*, 13(10):845–848, 2016.
- Haghverdi, L., Lun, A. T. L., Morgan, M. D., and Marioni, J. C. Batch effects in single-cell RNA-sequencing data are corrected by matching mutual nearest neighbors. *Nature Biotechnology*, 36(5):421–427, May 2018. ISSN 1546-1696. doi: 10.1038/nbt.4091.
- Halmos, P., Gold, J., Liu, X., and Raphael, B. Hierarchical Refinement: Optimal Transport to Infinity and Beyond. In *Forty-Second International Conference on Machine Learning*, June 2025.
- Ham, J., Lee, D., and Saul, L. Semisupervised alignment of manifolds. In *International Workshop on Artificial Intelligence and Statistics*, pp. 120–127. PMLR, 2005.
- Ham, J. H., Lee, D. D., and Saul, L. K. Learning high dimensional correspondences from low dimensional manifolds. *Submitted for publication*, 2003.
- Hassine, K., Erbad, A., and Hamila, R. Important complexity reduction of random forest in multi-classification problem. In *2019 15th International Wireless Communications & Mobile Computing Conference (IWCMC)*, pp. 226–231. IEEE, 2019.
- Hie, B., Bryson, B., and Berger, B. Efficient integration of heterogeneous single-cell transcriptomes using Scanorama. *Nature Biotechnology*, 37(6):685–691, June 2019. ISSN 1546-1696. doi: 10.1038/s41587-019-0113-3.
- Indyk, P. and Motwani, R. Approximate nearest neighbors: Towards removing the curse of dimensionality. In *Proceedings of the Thirtieth Annual ACM Symposium on Theory of Computing*, pp. 604–613, 1998.
- Korsunsky, I., Millard, N., Fan, J., Slowikowski, K., Zhang, F., Wei, K., Baglaenko, Y., Brenner, M., Loh, P.-r., and Raychaudhuri, S. Fast, sensitive and accurate integration of single-cell data with Harmony. *Nature Methods*, 16(12):1289–1296, December 2019. ISSN 1548-7105. doi: 10.1038/s41592-019-0619-0.
- Leek, J. T., Scharpf, R. B., Bravo, H. C., Simcha, D., Langmead, B., Johnson, W. E., Geman, D., Baggerly, K., and Irizarry, R. A. Tackling the widespread and critical impact of batch effects in high-throughput data. *Nature Reviews Genetics*, 11(10):733–739, 2010. doi: 10.1038/nrg2825.
- Lindenbaum, O., Stanley, J., Wolf, G., and Krishnaswamy, S. Geometry based data generation. *Advances in Neural Information Processing Systems*, 31, 2018.
- Liu, J., Huang, Y., Singh, R., Vert, J.-P., and Noble, W. S. Jointly Embedding Multiple Single-Cell Omics Measurements. *Algorithms in bioinformatics : ... International Workshop, WABI ..., proceedings. WABI (Workshop)*, 143: 10, September 2019. doi: 10.4230/LIPIcs.WABI.2019.10.
- Loupe, G. *Understanding Random Forests: From Theory to Practice*. Universite de Liege (Belgium), 2014.
- Luecken, M. D., Büttner, M., Chaichoompu, K., Danese, A., Interlandi, M., Mueller, M. F., Strobl, D. C., Zappia, L., Dugas, M., Colomé-Tatché, M., and Theis, F. J. Benchmarking atlas-level data integration in single-cell genomics. *Nature Methods*, 19(1):41–50, January 2022. ISSN 1548-7105. doi: 10.1038/s41592-021-01336-8.
- Mémoli, F. Gromov–Wasserstein distances and the metric approach to object matching. *Foundations of computational mathematics*, 11(4):417–487, 2011.
- Moon, K. R., van Dijk, D., Wang, Z., Gigante, S., Burkhardt, D. B., Chen, W. S., Yim, K., van den Elzen, A., Hirn, M. J., Coifman, R. R., Ivanova, N. B., Wolf, G., and Krishnaswamy, S. Visualizing structure and transitions in high-dimensional biological data. *Nature Biotechnology*, 37(12):1482–1492, December 2019. ISSN 1546-1696. doi: 10.1038/s41587-019-0336-3.

- Pedregosa, F., Varoquaux, G., Gramfort, A., Michel, V., Thirion, B., Grisel, O., Blondel, M., Prettenhofer, P., Weiss, R., Dubourg, V., Vanderplas, J., Passos, A., Cournapeau, D., Brucher, M., Perrot, M., and Duchesnay, E. Scikit-learn: Machine learning in Python. *Journal of Machine Learning Research*, 12:2825–2830, 2011.
- Peyré, G., Cuturi, M., et al. Computational optimal transport: With applications to data science. *Foundations and Trends® in Machine Learning*, 11(5-6):355–607, 2019.
- Rand, W. M. Objective criteria for the evaluation of clustering methods. *Journal of the American Statistical Association*, 66(336):846–850, 1971. doi: 10.1080/01621459.1971.10482356. URL <https://www.tandfonline.com/doi/abs/10.1080/01621459.1971.10482356>.
- Rautenstrauch, P. and Ohler, U. Shortcomings of silhouette in single-cell integration benchmarking. *Nature Biotechnology* 2025, pp. 1–5, 7 2025. ISSN 1546-1696. doi: 10.1038/s41587-025-02743-4. URL <https://www.nature.com/articles/s41587-025-02743-4>.
- Rhodes, a. S. and Rustad, A. G. Graph Integration for Diffusion-Based Manifold Alignment. In *2024 International Conference on Machine Learning and Applications (ICMLA)*, pp. 1–8, December 2024a. doi: 10.1109/ICMLA61862.2024.00026.
- Rhodes, J. S. and Rustad, A. G. Random Forest-Supervised Manifold Alignment. In *2024 IEEE International Conference on Big Data (BigData)*, pp. 3309–3312, December 2024b. doi: 10.1109/BigData62323.2024.10825663.
- Rhodes, J. S., Aumon, A., Morin, S., Girard, M., Laroche, C., Brunet-Ratnasingham, E., Pagliuzza, A., Marchitto, L., Zhang, W., Cutler, A., et al. Gaining biological insights through supervised data visualization. *bioRxiv : the preprint server for biology*, pp. 2023–11, 2023a.
- Rhodes, J. S., Cutler, A., and Moon, K. R. Geometry- and Accuracy-Preserving Random Forest Proximities. *IEEE Transactions on Pattern Analysis and Machine Intelligence*, 45(9):10947–10959, September 2023b. ISSN 1939-3539. doi: 10.1109/TPAMI.2023.3263774.
- Rousseeuw, P. J. Silhouettes: A graphical aid to the interpretation and validation of cluster analysis. *Journal of Computational and Applied Mathematics*, 20:53–65, 11 1987. ISSN 0377-0427. doi: 10.1016/0377-0427(87)90125-7. URL <https://www.sciencedirect.com/science/article/pii/0377042787901257>.
- Scetbon, M., Cuturi, M., and Peyré, G. Low-Rank Sinkhorn Factorization. In *Proceedings of the 38th International Conference on Machine Learning*, pp. 9344–9354. PMLR, July 2021.
- Stuart, T., Butler, A., Hoffman, P., Hafemeister, C., Papalexi, E., Mauck, W. M., Hao, Y., Stoeckius, M., Smibert, P., and Satija, R. Comprehensive integration of single-cell data. *Cell*, 177(7):1888–1902, 2019. doi: 10.1016/j.cell.2019.05.031.
- Tan, S., Soloviev, M., Hooker, G., and Wells, M. T. Tree Space Prototypes: Another Look at Making Tree Ensembles Interpretable. In *Proceedings of the 2020 ACM-IMS on Foundations of Data Science Conference, FODS '20*, pp. 23–34, New York, NY, USA, October 2020. Association for Computing Machinery. ISBN 978-1-4503-8103-1. doi: 10.1145/3412815.3416893.
- Thompson, B. *Canonical Correlation Analysis: Uses and Interpretation*, volume 47. Sage, 1984.
- Tran, H. Q., Ang, K. S., Chevrier, M., Zhang, X., Lee, N. Y. S., Goh, M.-H., and Chen, J. A benchmark of batch-effect correction methods for single-cell rna-sequencing data. *Genome Biology*, 21(1):12, 2020. doi: 10.1186/s13059-019-1850-9.
- Tuia, D. and Camps-Valls, G. Kernel Manifold Alignment for Domain Adaptation. *PLOS ONE*, 11(2):e0148655, February 2016. ISSN 1932-6203. doi: 10.1371/journal.pone.0148655.
- Vieira Braga, F. A., Kar, G., Berg, M., Carpaij, O. A., Polanski, K., Simon, L. M., Brouwer, S., Gomes, T., Hesse, L., Jiang, J., Fasouli, E. S., Efremova, M., Vento-Tormo, R., Talavera-López, C., Jonker, M. R., Affleck, K., Palit, S., Strzelecka, P. M., Firth, H. V., Mahbubani, K. T., Cvejic, A., Meyer, K. B., Saeb-Parsy, K., Luinge, M., Brandsma, C.-A., Timens, W., Angelidis, I., Strunz, M., Koppelman, G. H., van Oosterhout, A. J., Schiller, H. B., Theis, F. J., van den Berge, M., Nawijn, M. C., and Teichmann, S. A. A cellular census of human lungs identifies novel cell states in health and in asthma. *Nature Medicine*, 25(7):1153–1163, July 2019. ISSN 1546-170X. doi: 10.1038/s41591-019-0468-5.
- Wang, C. and Mahadevan, S. Manifold alignment using Procrustes analysis. In *Proceedings of the 25th International Conference on Machine Learning - ICML '08*, pp. 1120–1127, Helsinki, Finland, 2008. ACM Press. ISBN 978-1-60558-205-4. doi: 10.1145/1390156.1390297.
- Wang, C. and Mahadevan, S. Manifold alignment without correspondence. In *IJCAI*, volume 2, pp. 3, 2009.

- Wang, C. and Mahadevan, S. Heterogeneous domain adaptation using manifold alignment. In *IJCAI Proceedings-International Joint Conference on Artificial Intelligence*, volume 22, pp. 1541, 2011.
- Wang, J., Li, X., and Du, J. Label Space Embedding of Manifold Alignment for Domain Adaption. *Neural Process. Lett.*, 49(1):375–391, February 2019. ISSN 1370-4621. doi: 10.1007/s11063-018-9822-8.
- Welch, J. D., Kozareva, V., Ferreira, A., Vanderburg, C., Martin, C., and Macosko, E. Z. Single-cell multi-omic integration compares and contrasts features of brain cell identity. *Cell*, 177(7):1873, June 2019. doi: 10.1016/j.cell.2019.05.006.
- Xu, C., Lopez, R., Mehlman, E., Regier, J., Jordan, M. I., and Yosef, N. Probabilistic harmonization and annotation of single-cell transcriptomics data with deep generative models. *Molecular Systems Biology*, 17(1):MSB20209620, January 2021. ISSN 1744-4292. doi: 10.15252/msb.20209620.
- Zhu, J.-Y., Park, T., Isola, P., and Efros, A. A. Unpaired image-to-image translation using cycle-consistent adversarial networks. In *Proceedings of the IEEE International Conference on Computer Vision*, pp. 2223–2232, 2017.

A. Extended complexity analysis

Without loss of generality, assume balanced domains with $N = n = m$ samples each. FoSTA consists of three main stages: (i) computing label-informed RF-GAP affinities within each domain, (ii) estimating a cross-domain transport plan with HiRef in semantic space, and (iii) producing a joint low-dimensional embedding with Landmark PHATE.

Computing RF-GAP within a domain has time complexity $\mathcal{O}(TN \log N \cdot p + TN(h + \ell))$, where T is the number of trees, p is the number of candidate features evaluated per split, $h \approx \log N$ is the average tree height, and ℓ is the average number of in-bag/out-of-bag leaf interactions per sample (Louppe, 2014; Hassine et al., 2019). The associated memory footprint scales as $\mathcal{O}(NT(1 + \ell))$ for storing the sparse leaf-based interactions used to assemble affinities (Aumon et al., 2026). HiRef computes an approximately bijective Monge map in log-linear time and linear space in N (Halmos et al., 2025). Finally, Landmark PHATE with M landmarks builds landmark relationships at cost $\mathcal{O}(2NM)$ and stores them in $\mathcal{O}(2NM)$ memory, followed by diffusion and embedding on the landmark set, which costs $\mathcal{O}(M^3)$ (Moon et al., 2019; Demaine et al., 2021).

In general, T , p , and ℓ are treated as small constants relative to N , and $M \ll N$ is set to $M = 2000$ by default (Moon et al., 2019). Under these assumptions, FoSTA has effectively near-linear (log-linear) runtime and linear memory scaling in the number of samples. In contrast, MALI and related OT-based alignment methods rely on full DPT and/or explicit dense cross-domain cost matrices, leading to at least quadratic time and space complexity in N .

B. Description of the benchmark datasets

Here, we describe the 15 datasets from the [UCI Machine Learning Repository](#) used to evaluate multimodal data integration performance in Section 4.1. Following the experimental protocol of Rhodes & Rustad (2024b), we select the Balance Scale, Breast Cancer, CRX, Diabetes, E. coli (restricted to five majority classes), Flare1, Glass, Heart Disease, Heart Failure, Hepatitis, Ionosphere, Iris, Parkinson’s, Seeds, and Tic-Tac-Toe datasets. Table 2 summarizes each dataset, including the number of observations, features, and classes.

Table 2. Summary of the datasets used to evaluate multimodal data integration performance in Section 4.1. Observations with missing values were removed prior to analysis.

	Balance Scale	Breast Cancer	CRX	Diabetes	E. coli	Flare1	Glass	Heart Disease	Heart Failure	Hepatitis	Ionosphere	Iris	Parkinson’s	Seeds	Tic-Tac-Toe
# Observations	625	699	664	678	336	323	214	303	299	138	351	150	195	199	958
# Features	4	16	14	8	8	10	9	13	10	15	34	4	22	7	9
# Classes	3	2	2	2	5	3	6	5	2	2	2	3	2	3	2

C. Description of metrics used in the batch effect removal task.

The implementation of all metrics for batch correction and bio conservation is taken from the scib-metrics package (Luecken et al., 2022). All metrics are normalized and transformed appropriately so that the result lies between 0 and 1, with higher score corresponding to better performance.

For all definitions, we assume the following notation. Denote the dataset by $\mathcal{D} = \{x_1, \dots, x_n\}$, with $x_i \in \mathbb{R}^d$ for all i . Let $X \in \mathbb{R}^{n \times d}$ denote the data matrix, with samples in the rows and n denoting the number of samples. Let $\mathcal{L} = \{1, \dots, n_l\}$ denote a set of n_l (encoded) labels, which could be the cell type labels or the batch label, depending on the case, and let $L \in \mathcal{L}^n$ denote the vector of labels for each sample.

C.1. Biological conservation metrics

Normalized mutual information (NMI; Danon et al. (2005)) and Adjusted Rand index (ARI; Rand (1971)) measure the preservation of clustering, i.e. how well a clustering of the integrated data overlap with the cell type labels.

NMI is computed as follows. Let $\mathcal{C} = \{1, \dots, n_c\}$ denote a set of n_c clusters in the embedding under evaluation, and let

$C \in \mathcal{C}^n$ denote the vector of cluster assignment for each sample. Let N be the confusion matrix with rows corresponding to cell type labels, and columns corresponding to clusters in the embedding under evaluation, with entries n_{lc} equal to the number of samples with cell type label l that appear in cluster c of the embedding. Now let $n_l = \sum_i n_{li}$ denote the total number of samples in cell type l , $n_{\cdot c} = \sum_i n_{ic}$ denote the total number of samples in cluster c , and $n = \sum_{ij} n_{ij}$ denote the total number of cells.

Then, the mutual information of labels and clusters in the confusion matrix N is given by

$$\text{MI}(L, C) = \sum_{l \in \mathcal{L}} \sum_{c \in \mathcal{C}} n_{lc} \log \frac{n \cdot n_{lc}}{n_{\cdot c} n_l}.$$

Define the entropy of the cell type labels as $H(L) = - \sum_{l \in \mathcal{L}} n_l \cdot \log(n_l/n)$, and the entropy of the clusters as $H(C) = - \sum_{c \in \mathcal{C}} n_{\cdot c} \log(n_{\cdot c}/n)$. Then,

$$\text{NMI}(L, C) = \frac{2 \cdot \text{MI}(N)}{H(L) + H(C)}.$$

Leiden NMI is NMI computed with C from Leiden clustering on the embedding, while **KMeans NMI** is computed with C from k -means clustering, where k is set to the number of cell types.

ARI is another metric to evaluate the alignment of two clusterings, based on comparing the amount of agreement to that of a random clustering. Let

$$n_{\text{agreements}} = \sum_{i,j} \mathbb{I}(L_i = L_j \text{ and } C_i = C_j) + \sum_{i,j} \mathbb{I}(L_i \neq L_j \text{ and } C_i \neq C_j).$$

Define the number of true positives n_{tp} , false positives n_{fp} , true negatives n_{tn} , and false negatives n_{fn} as

$$\begin{aligned} n_{\text{tp}} &= \sum_{i,j} \mathbb{I}(L_i = L_j \text{ and } C_i = C_j), & n_{\text{fp}} &= \sum_{i,j} \mathbb{I}(L_i \neq L_j \text{ and } C_i = C_j), \\ n_{\text{tn}} &= \sum_{i,j} \mathbb{I}(L_i \neq L_j \text{ and } C_i \neq C_j), & n_{\text{fn}} &= \sum_{i,j} \mathbb{I}(L_i = L_j \text{ and } C_i \neq C_j). \end{aligned}$$

The ARI is then given by [Pedregosa et al. \(2011\)](#):

$$\text{ARI}(L, C) = \frac{2(n_{\text{tp}}n_{\text{tn}} - n_{\text{fn}}n_{\text{fp}})}{(n_{\text{tp}} + n_{\text{fn}}) \cdot (n_{\text{tn}} + n_{\text{fp}}) + (n_{\text{tp}} + n_{\text{fp}}) \cdot (n_{\text{tn}} + n_{\text{fn}})}.$$

Computing ARI with C from Leiden clustering or k -means clustering, with k set to the number of cell types, gives rise **Leiden ARI**, and **KMeans ARI** respectively.

Silhouette label evaluates cell type separation in the integrated embedding. It is computed with the Average Silhouette Width (ASW; [Rousseeuw \(1987\)](#)) of cell types, i.e. the average over all samples i of

$$\text{ASW}(L) = \frac{1}{n} \sum_{i \in \mathcal{D}} s(i) = \frac{1}{n} \sum_{i \in \mathcal{D}} \frac{b(i) - a(i)}{\max\{a(i), b(i)\}},$$

where

$$a(i) = \frac{1}{|\{j \in \mathcal{D} | L_j = L_i\}|} \sum_{j \in \mathcal{D} | L_j = L_i} d(i, j)$$

denotes the average distance to cells in the same cluster, and

$$b(i) = \min_{L_k \neq L_i} \frac{1}{|\{j \in \mathcal{D} | L_j = L_k\}|} \sum_{j \in \mathcal{D} | L_j = L_k} d(i, j)$$

denotes the minimum average distance to another cluster. For silhouette label, L is the vector of cell type labels.

cLISI is based on the local Inverse Simpson's Index (LISI) is a measure of diversity that captures how many samples must be drawn from a neighborhood of a sample before drawing a duplicate label. For each cell, a probability distribution p_i over its neighborhood is defined based on a Gaussian kernel of the distances to the cell of interest. Then

$$\text{LISI} = \text{median}_{i \in \mathcal{D}} \frac{1}{\sum_{l \in \mathcal{L}} p_i(l)},$$

where $p_i(l) = \sum_j p_i(j) \mathbb{I}(L_j = l)$. The result is transformed so that high scores correspond to low cell type diversity (high purity). **cLISI** (Korsunsky et al., 2019) is the LISI where L is the cell types, measuring the level of cell type mixing that occurs in the neighborhoods of all cells.

The **isolated labels** metric evaluates the separation of isolated labels, defined as labels that are present in the fewest batches, from other labels. It is computed as the ASW of the isolated labels versus the other labels.

C.2. Batch correction metrics

Batch removal adapted silhouette (**BRAS**; Rautenstrauch & Ohler (2025)) is an adaptation of ASW where L is the batch identity labels that is better suited to evaluate batch mixing and nested batch effects. BRAS is defined like ASW, except that $b(i)$ is defined as the mean distance to cells in other clusters: $b(i) = \frac{1}{|\{j \in \mathcal{D} | L_j \neq L_k\}|} \sum_{j \in \mathcal{D} | L_j \neq L_k} d(i, j)$.

Then,

$$\text{BRAS} = \frac{1}{n_l} \sum_{l \in \mathcal{L}} \left[\frac{1}{|\{i \in \mathcal{D} | L_j = l\}|} \sum_{\{i \in \mathcal{D} | L_j = l\}} (1 - |s(i)|) \right]$$

iLISI (Korsunsky et al., 2019) is the median of LISI applied to the batch labels (see section C.1).

kBET (Büttner et al., 2019) performs statistical tests to determine whether local composition of neighborhoods in terms of batch labels corresponds to the global batch distribution. The output is the average rejection rate of the null hypothesis (complete batch mixing) computed over the neighborhoods of samples selected at random. Here, kBET is computed separately for each cell type, and then averaged over all cell types:

$$\text{kBET}(\mathcal{D}) = \frac{1}{n_l} \sum_{l \in \mathcal{L}} \text{kBET}(l) = \frac{1}{n_l} \sum_{l \in \mathcal{L}} \left(\frac{1}{|\mathcal{Y}|} \sum_{i \in \mathcal{Y}} S_i^l \right),$$

where S_i^l is the rejection rate of the statistical test on the batch labels of a neighborhood centered at i restricted to cells with label l , and $\mathcal{Y} \subset \mathcal{D}$ is a random subset of samples.

Graph connectivity measures for each label l the connectivity of a k nn graph G_l subset to only the samples of label l , i.e.

$$GC = \frac{1}{|\mathcal{L}|} \sum_{l \in \mathcal{L}} \frac{|LCC(G_l)|}{n_l},$$

where LCC denotes the largest connected component of a graph and n_l denotes the number of samples with label l .

Principal Component Regression (**PCR**) comparison (Büttner et al., 2019) measures the variance explained by the batch. It is based on Principal component analysis (PCA), which returns n principal components (PC). By fitting a linear regression of the batches on the i th PC, we obtain an R^2 value, denoted R_i^2 . The total variance explained by the batch is the weighted average over all PCs of the variance explained by the PC with the R^2 of the batch on this PC:

$$\text{Var} = \sum_i \text{Var}_i \cdot R_i^2,$$

where Var_i denotes the variance of the data matrix X explained by the i th principal component.

D. Extension to imbalanced domain sizes

We focused on the balanced setting, assuming full overlap between the two domains. In practice, however, many applications involve imbalanced domain sizes ($n \neq m$). Several strategies can be employed to extend our framework to this more general setting.

Recall that in the balanced case, correspondence matching is formulated using HiRef, which seeks a Monge map between domains and therefore enforces a bijection. In the imbalanced setting, this naturally generalizes to seeking an *injection* from the smaller domain into the larger one. Two straightforward approaches follow from this formulation. First, the larger domain can be subsampled to match the size of the smaller domain prior to alignment. Alternatively, the smaller domain can be augmented with *dummy points* to absorb excess mass from the larger domain during transport (Caffarelli & McCann, 2010; Chapel et al., 2020).

Another simple yet powerful strategy consists in oversampling the smaller domain directly in the input feature space using methods such as SMOTE (Chawla et al., 2002) or SUGAR (Lindenbaum et al., 2018). While effective in some settings, this approach may propagate noise in highly heterogeneous or noisy datasets. A more robust alternative would therefore be to perform such augmentation in the forest leaf-induced representation space, where task-relevant structure has already been denoised.

We leave a full treatment of imbalanced domain alignment within the FoSTA framework for future work.

E. Complete results in the batch effect correction task

Here we provide the full results for all methods and metrics in the batch effect correction task described in Section 4.2. Table 3 gives the batch correction metrics while Table 4 gives the biological conservation metrics.

Table 3. Complete results of all batch correction metrics in the lung batch integration task.

Model	BRAS	iLISI	KBET	Graph connectivity	PCR comparison
MALI	0.345 ± 0.094	0.893 ± 0.039	0.447 ± 0.257	0.503 ± 0.073	0.997 ± 0.028
FoSTA	0.382 ± 0.062	0.693 ± 0.135	0.602 ± 0.135	0.727 ± 0.054	0.991 ± 0.028
Scanorama	0.182 ± 0.160	0.096 ± 0.249	0.170 ± 0.242	0.461 ± 0.137	0.139 ± 0.296
Harmony	0.504 ± 0.244	0.102 ± 0.233	0.500 ± 0.313	0.521 ± 0.153	0.564 ± 0.438
scVI	0.582 ± 0.039	0.946 ± 0.004	0.959 ± 0.022	0.798 ± 0.038	0.932 ± 0.213
scANVI	0.613 ± 0.043	0.946 ± 0.003	0.959 ± 0.018	0.896 ± 0.042	0.961 ± 0.116
Pamona	0.615 ± 0.064	0.367 ± 0.181	0.259 ± 0.218	0.529 ± 0.078	1.000 ± 0.001
KEMArbf	0.362 ± 0.050	0.747 ± 0.124	0.333 ± 0.192	0.564 ± 0.054	0.785 ± 0.364
KEMAlin	0.369 ± 0.099	0.510 ± 0.241	0.162 ± 0.129	0.510 ± 0.070	0.863 ± 0.194
Uncorrected	0.452 ± 0.212	0.049 ± 0.169	0.304 ± 0.299	0.522 ± 0.152	0.000 ± 0.000

Table 4. Complete results of all biological conservation metrics in the lung batch integration task.

Model	Isolated labels	Leiden NMI	Leiden ARI	KMeans NMI	KMeans ARI	Silhouette label	cLISI
MALI	0.444 ± 0.055	0.370 ± 0.129	0.166 ± 0.071	0.459 ± 0.199	0.377 ± 0.245	0.453 ± 0.098	0.974 ± 0.029
FoSTA	0.586 ± 0.053	0.551 ± 0.031	0.235 ± 0.022	0.779 ± 0.065	0.767 ± 0.111	0.798 ± 0.085	1.000 ± 0.000
Scanorama	0.427 ± 0.059	0.476 ± 0.053	0.243 ± 0.031	0.484 ± 0.055	0.251 ± 0.031	0.406 ± 0.108	0.997 ± 0.003
Harmony	0.510 ± 0.062	0.708 ± 0.151	0.631 ± 0.227	0.543 ± 0.077	0.311 ± 0.071	0.505 ± 0.079	0.997 ± 0.006
scVI	0.548 ± 0.021	0.562 ± 0.017	0.245 ± 0.019	0.555 ± 0.018	0.261 ± 0.019	0.549 ± 0.039	1.000 ± 0.000
scANVI	0.693 ± 0.035	0.601 ± 0.016	0.266 ± 0.022	0.614 ± 0.015	0.322 ± 0.026	0.648 ± 0.034	1.000 ± 0.000
Pamona	0.463 ± 0.023	0.362 ± 0.165	0.164 ± 0.139	0.365 ± 0.187	0.207 ± 0.160	0.517 ± 0.044	0.982 ± 0.017
KEMArbf	0.451 ± 0.060	0.505 ± 0.082	0.236 ± 0.051	0.706 ± 0.207	0.704 ± 0.297	0.748 ± 0.077	0.996 ± 0.013
KEMAlin	0.461 ± 0.061	0.470 ± 0.112	0.220 ± 0.066	0.519 ± 0.126	0.319 ± 0.093	0.548 ± 0.041	0.989 ± 0.023
Uncorrected	0.502 ± 0.059	0.672 ± 0.147	0.567 ± 0.220	0.535 ± 0.075	0.299 ± 0.069	0.492 ± 0.073	0.997 ± 0.007